








RESEARCH ARTICLE | JULY 09 2024

# Highly flexible and temperature-tolerant phase change devices for dual-band camouflage

Liuxiang Huo (霍柳香) ; Lin Wang (王林); Shubing Li (李树兵); Xionghu Xu (许雄虎);  
Liangqing Zhu (朱亮清) ; Yawei Li (李亚巍) ; Liyan Shang (商丽燕) ; Kai Jiang (姜凯) ;  
Junhao Chu (褚君浩); Zhigao Hu (胡志高)  

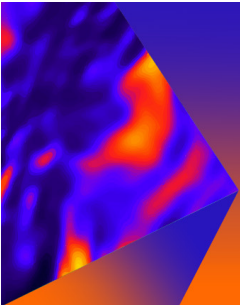
 Check for updates

*Appl. Phys. Rev.* 11, 031403 (2024)

<https://doi.org/10.1063/5.0199932>




09 July 2024 22:48:54

**Applied Physics Letters**

Special Topic: Mid and Long Wavelength Infrared Photonics, Materials, and Devices

**Submit Today**



# Highly flexible and temperature-tolerant phase change devices for dual-band camouflage

Cite as: Appl. Phys. Rev. **11**, 031403 (2024); doi: [10.1063/5.0199932](https://doi.org/10.1063/5.0199932)

Submitted: 24 January 2024 · Accepted: 10 June 2024 ·

Published Online: 9 July 2024






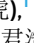
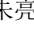

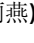
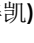

View Online



Export Citation



CrossMark

Liuxiang Huo (霍柳香),<sup>1</sup>  Lin Wang (王林),<sup>1</sup>  Shubing Li (李树兵),<sup>1</sup>  Xionghu Xu (许雄虎),<sup>1</sup>  Liangqing Zhu (朱亮清),<sup>1,a)</sup>   
Yawei Li (李亚巍),<sup>1</sup>  Liyan Shang (商丽燕),<sup>1</sup>  Kai Jiang (姜凯),<sup>1,2</sup>  Junhao Chu (褚君浩),<sup>1,3</sup>  
and Zhigao Hu (胡志高)<sup>1,3,b)</sup> 

## AFFILIATIONS

<sup>1</sup>Technical Center for Multifunctional Magneto-Optical Spectroscopy (Shanghai), Engineering Research Center of Nanophotonics and Advanced Instrument (Ministry of Education), Department of Materials, School of Physics and Electronic Science, East China Normal University, Shanghai 200241, China

<sup>2</sup>School of Arts and Sciences, Shanghai Dianji University, Shanghai 200240, China

<sup>3</sup>Collaborative Innovation Center of Extreme Optics, Shanxi University, Taiyuan, Shanxi 030006, China

<sup>a)</sup>Electronic mail: [lqzhu@ee.ecnu.edu.cn](mailto:lqzhu@ee.ecnu.edu.cn)

<sup>b)</sup>Author to whom correspondence should be addressed: [zghu@ee.ecnu.edu.cn](mailto:zghu@ee.ecnu.edu.cn)

## ABSTRACT

Here, we have developed a more temperature-tolerant emitter with a gradient emittance, which can enable adaptation to changing environmental conditions. Such a thermal emitter is mainly constructed by multilayered films composed of nitrogen (N)-doped  $\text{Ge}_2\text{Sb}_2\text{Te}_5$  (N-GST) and an underlying metal film. The proposed device not only possesses special wavelength selectivity in the middle infrared range but can also dynamically adjust average emissivity (from 0.13 to 0.83) through the degree of crystallization. Besides, N doping can elevate the phase transition temperature of GST and enhance its thermal resistance, which renders it particularly well-suited for applications in higher temperature environments than pure GST. This emitter also shows strong adhesion capability and high flexibility against bending, enabling more practical and widespread situations. By using a multi-layer structure, we combined the more temperature-tolerant and dynamically modulating N-GST emitter with an optical thin film, successfully achieving dual camouflage for both infrared and visible light. The element doping technology and multi-layer stacking approach presented in this research will provide valuable insight for the development of dynamic emissive materials in multi-spectral camouflage scenarios.

Published under an exclusive license by AIP Publishing. <https://doi.org/10.1063/5.0199932>

## I. INTRODUCTION

To protect themselves from predators, various creatures in nature, such as chameleons, squid, cuttlefish, and other animals, possess the remarkable ability to alter their coloration.<sup>1–3</sup> When tracked, they seamlessly blend into their surroundings. This visual camouflage greatly improves their survivability and finds application in human development, including electrochromic materials,<sup>4</sup> electromagnetic communication,<sup>5</sup> coating materials,<sup>6,7</sup> temperature control,<sup>8,9</sup> and various other applications.<sup>10–12</sup> In the infrared range, similar to color camouflage in the visible spectrum, this ability is termed “thermal camouflage.”<sup>13,14</sup> All objects at a temperature above absolute zero will give off a thermal signal, which can be mainly captured and localized by mid-infrared (MIR) cameras.<sup>15,16</sup> However, when the objects themselves can align with the background’s radiative temperature, the difference in their thermal emission intensities evades observation, thus

effectively confronting infrared detection. According to the Stefan-Boltzmann law, an object’s thermal radiation is determined by its surface’s infrared emissivity ( $\epsilon$ ) and its surface thermodynamic temperature ( $T$ ) to the fourth power ( $P = \sigma \epsilon T^4$ , where  $\sigma$  is the Stefan-Boltzmann constant).<sup>17</sup> Adjusting the surface emissivity to match the thermal radiation energy emitted by the target object with that of the background becomes a crucial approach to achieving thermal camouflage,<sup>18–20</sup> thereby integrating it with the environment.

Low emissivity coatings or films are effective in reducing thermal radiation and are commonly used in situations where the target’s temperature exceeds that of the surroundings. However, traditional broad-spectrum infrared camouflage, reliant on fixed emissivity, is easily detectable due to its inability to adjust to varying background temperatures. The dynamic camouflage capability, characterized by the ability of actual emissivity to adapt to changes in background temperature,

possesses broader practicality and holds promising prospects for wider applications. Recent studies have explored various composite materials for dynamic thermal camouflage, including graphene, ferroelectric substances, nanoscale metamaterials, phase change materials, etc. For instance, graphene offers precise active control adjustment, but its high defect density limits its thermal regulation capability.<sup>21–24</sup> Active metasurfaces achieve spatiotemporal control of spectral emissivity by optically modulating carrier concentration, yet their adjustment range remains limited.<sup>25</sup> Similarly, the optical excitation of ZnO nanocrystals only achieves limited emissivity variation.<sup>26</sup> These modulation methods can only achieve bistable adjustment with a low modulation range, thus failing to meet the wide modulation range required for continuous adjustability of emissions.

Phase change materials (PCMs) have been extensively studied for their dynamic emissivity control and broad modulation range. Among them, sulfur-based  $\text{Ge}_2\text{Sb}_2\text{Te}_5$  (GST) is a typical phase change infrared stealth material that can alter its internal atomic structure through stimuli such as heat, lasers, and voltage.<sup>27–29</sup> GST exhibits distinct changes in resistivity and optical properties before and after phase transition, making it suitable for active control of infrared stealth.<sup>30,31</sup> Doping has been used to optimize GST performance, such as substituting selenium for Te to reduce optical losses and improve the application effectiveness of light switches.<sup>32</sup> Multielement doping also contributes to enhancing GST's thermal stability, making it more suitable for higher temperature environments.<sup>33–35</sup> Recent research has shown that GST PCM can achieve thermal camouflage by controlling the ratio of crystalline and amorphous phases, effectively concealing at different background temperatures.<sup>36</sup> So far, many GST-based emitters have demonstrated promising application potential in encryption, camouflage, and related fields.<sup>37,38</sup> However, several studies indicate that GST, due to its relatively fixed and low phase transition temperature ( $\sim 150^\circ\text{C}$ ),<sup>39,40</sup> struggles to withstand certain higher temperature devices. Currently, the main methods applied in high-temperature camouflage scenarios involve using aerogel insulation layers or introducing porous structures into materials like Mxene and ceramics.<sup>39,41,42</sup> This is because hindering heat transfer results in significantly lower surface temperatures of the covering layer than the actual object temperature, thereby weakening the infrared radiation. Nonetheless, the adoption of thick aerogel layers is not conducive to adherence to complex surfaces. Moreover, the role of porous structures in improving the heat resistance of GST, which varies with temperature, is limited. Therefore, doping strategies are more advantageous for GST to match higher temperature stealth scenarios.

To camouflage objects within the recently developed advanced detectors operating across various wavelength bands, the compatibility of camouflage across different spectral bands is further explored.<sup>43–45</sup> For different camouflage principles in different bands, the device needs to satisfy the following requirements: (i) Infrared camouflage, especially in the MIR region of  $8\text{--}14\ \mu\text{m}$ , aims to achieve similar infrared radiance with the surrounding environment.<sup>46–48</sup> (ii) Visible camouflage ( $380\text{--}780\ \text{nm}$ ) aims to modify the characteristic reflection for background matching.<sup>49,50</sup> (iii) Microwave camouflage primarily aims to increase absorbance in the microwave radar band to reduce the reflected radar signal.<sup>51,52</sup> Previously, photonic crystals and metasurfaces were believed to possess multi-band compatible camouflage capabilities.<sup>53–59</sup> For instance, layered-designed camouflage devices achieved multispectral camouflage, while microwave stealth structures

were based on the phase cancellation of microwave scattering. Camouflage in the visible and infrared bands relied on the silicon–aluminum layered structure of low emissivity Lambertian surfaces.<sup>60</sup> However, their fabrication process is complex and difficult, and the emissivity characteristics of most designs remain unchanged. Laser-induced color change based on the GST layer is singular and mainly used for visible-infrared anti-counterfeiting purpose, failing to match the visible camouflage needs of diverse natural environments.<sup>37</sup> Therefore, it is of great significance to explore the use of films with active emissivity modulation to achieve multi-band compatible camouflage and thermal management.

In this study, we prepared a nitrogen-doped GST (N-GST) layer as an adaptive infrared transmitter for the application of infrared camouflage, aiming to improve the temperature resistance of GST. Doping modification strategies have been extensively used in PCM to optimize various characteristics, such as crystallization speed, resistivity, thermal stability, grain size, and service life. However, the specific infrared camouflage capabilities of modified GST on objects have not been thoroughly explored. This work focuses on investigating the actual impact of N doping on the phase transition temperature and temperature tolerance of GST and the characterization of N-GST. Compared to other static infrared stealth coatings, N-GST exhibits dynamic modulation effects. This material is prepared using magnetron sputtering, a simple manufacturing process that allows for large-scale production without the need for photolithography, offering design flexibility. Furthermore, N-GST has a broader emissivity modulation range (0.7), making it superior to GST and most dynamic radiation devices. The increased phase transition temperature and thermal stability significantly expand the application range of N-GST. Through bending experiments with N-GST attached to a flexible substrate, its suitability for various objects has been validated, providing feasibility for more practical and widespread applications. Additionally, combining N-GST with ZnS to form a multi-layer film structure achieves dual camouflage functionality for both the infrared and visible wavelength regions, offering promising prospects for future multispectral camouflage solutions.

## II. MATERIALS AND METHODS

### A. Fabrication of the device

All the silicon and polyimide substrates used are cleaned sequentially by ultrasonic cleaning with acetone, ethanol, and de-ionized water according to a standard process. As an adhesion layer, Cr metal layer with a thickness of 20 nm is magnetron sputtered onto the clean silicon wafer. As a reflector, a 100 nm thick Au film is deposited by thermal evaporation technique on Cr film. After that, the N-GST layer is deposited by radio frequency (RF) sputtering of an alloy target with an elemental content ratio of 2:2:5 for Ge, Te, and Sb under a mixed gas atmosphere of argon and nitrogen. The sputtering power is 40 W. The starting and working pressure are set to  $5 \times 10^{-4}$  and 0.8 Pa separately. As a comparison sample, GST is prepared similarly, but without the addition of nitrogen. The ZnS layer is fabricated by 30 W RF sputtering, with the starting pressure of  $5 \times 10^{-4}$  Pa and working pressure of 0.5 Pa. Both GST and ZnS are high-grade targets (99.99%). Since the optical thickness of the gold film is thick enough, the substrate could be various material systems as required.

## B. Characterization

X-ray diffraction (XRD, Japan SmartLab) with Cu K $\alpha$  radiation was used to measure the structural characteristics of thin films within the range from 20° to 60° and the scanning rate is 0.2°/s. X-ray photoelectron spectroscopy (XPS, Thermo ESCALAB 250XI) equipped with monochromatic Al K $\alpha$  (energy 1486.68 eV) was conducted to acquire the chemical valence and chemical composition of samples. Atomic force microscopy (AFM, Dimension Icon, Bruker) was applied to study the surface morphology of films and measure the film thickness. In addition, Raman spectroscopy (Jobin-Yvon LabRAM HR Evolution spectrometer) measurement was performed using a 532 nm laser in the frequency range of 50–300 cm<sup>-1</sup>. THMSE 600 heating/cooling stage (Linkam Scientific Instruments) was used to realize the temperature change tests. The transmittance and reflectivity of the films were recorded using a double-beam UV-vis-NIR spectrophotometer (PerkinElmer Lambda 950). X-ray spectroscopy (EDS) elemental mapping was captured using the STEM mode of JEM Grand ARM300F with a probe corrector and an EDS detector operated at 300 kV.

## C. Optical simulations and measurements

The finite-difference time-domain method (FDTD Solutions v8.13, Lumerical) is used to compute the optical responses of the thermal emitter. The relative permittivity of gold is obtained from Olmon's work.<sup>61</sup> The relative permittivities of N-GST (2.5–15  $\mu$ m) are obtained experimentally from the fabricated N-GST films. According to Kirchhoff's law of thermal radiation, the absorptivity at different incident angles are equal to the emissivity at the corresponding observation angles. The simulated emissivity can be replaced by the simulated absorptivity, and the observation angles can be replaced by the incident angles. The infrared images are recorded by an infrared camera (FLIR E8 XT). The spectral range of the infrared camera is between 7.5 and 13  $\mu$ m. The spectral radiance is measured by a Fourier transform infrared spectrometer (FTIR) (Bruker) with a deuterated lanthanum  $\alpha$ -alanine-doped triglycine sulfate (DLATGS) detector.

## III. RESULTS AND DISCUSSION

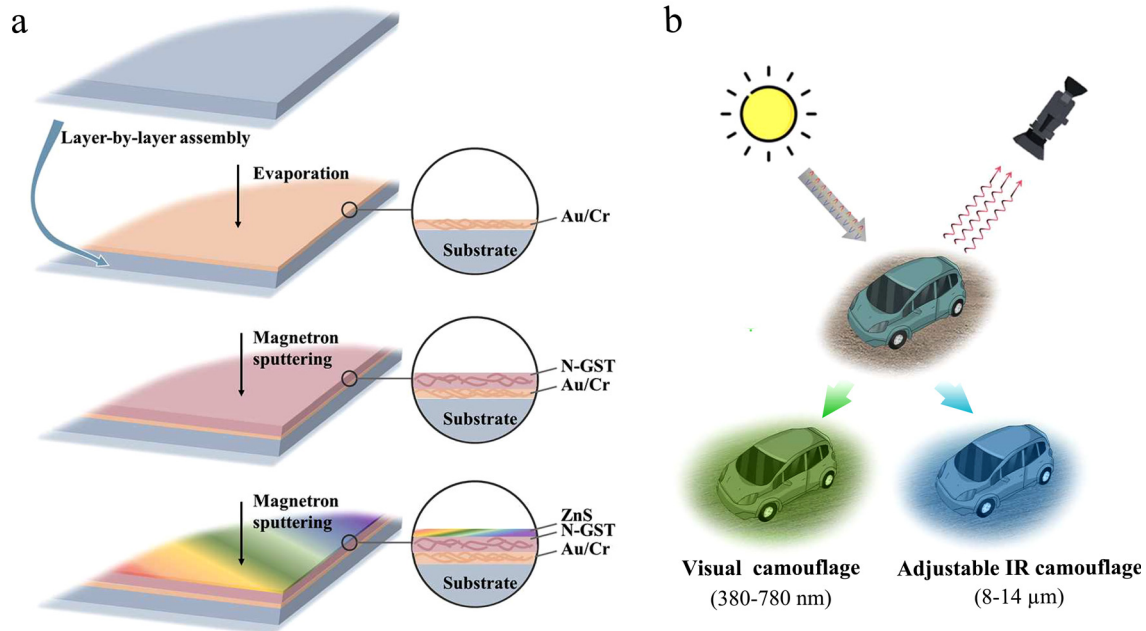
Figure 1(a) depicts the preparation process of a multilayered structure with dual-band spectral camouflage, achieved through the combination of the N-GST/Au thermal emitter and the ZnS membrane layer. The N-GST/Au thermal emitter comprises a 100 nm thick Au layer and a 540 nm thick N-GST layer. Initially, a 20 nm Cr metal layer was magnetron sputtered onto the substrate as an adhesion layer. A 100 nm thick Au back-reflector was deposited onto the substrate via thermal evaporation. It is worth noting that this thickness exceeds the penetration depth of both visible and infrared light for Au material. Subsequently, the N-GST layer was sputtered onto the Au film in a high vacuum environment at room temperature. This resulting N-GST/Au thermal emitter offers adjustable emittance within the infrared atmospheric window and demonstrates improved temperature resistance, thereby enhancing its thermal camouflage performance. In parallel, the ZnS film, intended for visible camouflage, was also achieved through magnetron sputtering. As displayed in Fig. 1(b), the combined structure fulfills the requirements for dual-band camouflage and exhibits a degree of temperature resistance. In many scenarios, ambient temperature fluctuations pose challenges in concealing objects with consistent temperatures using fixed low emissivity coatings. GST camouflage coatings with the ability to dynamically adjust emissivity

present difficulties for infrared cameras to discern object radiation from the background. However, the effectiveness of GST is hampered by its low phase change temperature and limited thermal stability. This study delves into improving the phase transition temperature by introducing a small amount of N doping in GST, aiming to enhance its practicality in achieving an effective infrared stealth effect.

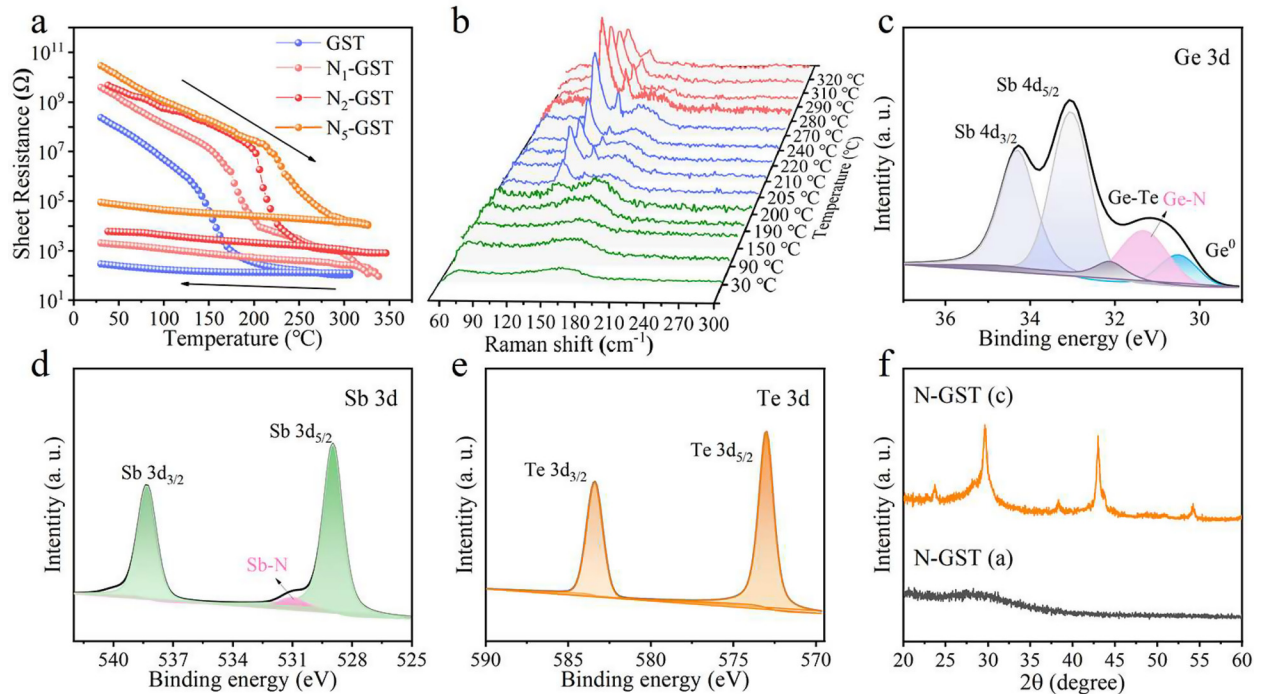
The impact of different N doping concentrations on the resistivity of GST can be demonstrated through electrical characteristics. Therefore, we conducted temperature-dependent resistance measurements ( $R$ - $T$ ) on N-GST thin films with different N concentrations. To prepare N-GST thin films, high-purity nitrogen gas was introduced during the magnetron sputtering process. Fixed nitrogen/argon flow ratios of 0:100, 1:99, 3:97, and 5:95 resulted in nitrogen contents of 0%, 8.6%, 12%, and 14%, respectively, denoted as GST, N<sub>1</sub>-GST, N<sub>3</sub>-GST, and N<sub>5</sub>-GST. However, higher N concentrations led to the depletion of Te, causing the film to deviate from the expected GST properties. The nitrogen content of the films, measured by the EDS method (shown in Table S1), remained relatively constant before and after the crystallization of thin film materials. It was also confirmed by the findings of Kolobov *et al.*<sup>62</sup> These samples underwent *in situ* variable-temperature resistance testing on a vacuum-heated probe table. Figure 2(a) displays *in situ* temperature-dependent testing curves during both the heating and cooling processes for N<sub>x</sub>-GST thin films. In the initial stage of the heating process, the resistance of N<sub>x</sub>-GST thin films with different compositions decreased gradually due to the thermally activated electron transition mechanism within the chalcogenide phase change materials. As the temperature approaches the crystallization point, the film resistance decreases sharply. With an increase in the nitrogen proportion, the  $R$ - $T$  curve gradually shifts to the right, suggesting that within a certain range of nitrogen concentrations, the crystallization temperature of N<sub>x</sub>-GST notably rises with increasing nitrogen doping. N<sub>5</sub>-GST demonstrates a crystallization temperature of 210 °C, which is 60 °C higher than that of pure GST,<sup>63</sup> making it suitable for thermal applications at higher temperatures. Subsequently, N<sub>5</sub>-GST, hereafter referred to as N-GST for simplicity, is further investigated as a thermal camouflage device.

Additionally, a variable-temperature Raman scattering test was conducted to elucidate the evolution mechanism of N-doped GST films during the phase transition. To prevent laser-induced sample crystallization, the laser intensity was set to 0.1 mW/mm<sup>2</sup>. Figure 2(b) illustrates the Raman spectrum of N-GST at room temperature, primarily displaying two broad peaks at 69.8 and 160.4 cm<sup>-1</sup>, associated with GeTe<sub>4</sub> tetrahedra and Sb-Te vibrations, respectively. Notably, the Raman spectra of amorphous films reveal red-shifted positions of these two broad peaks due to the effect of N doping as compared to pure GST.<sup>65</sup> Upon heating the film to approximately 205 °C, two new Raman peaks emerge while the intensity of the initial broad peaks diminishes. Another significant change occurs at 270 °C, with the initial broad peaks almost disappearing while the newly emerged peaks intensify. These distinct changes can be attributed to the transformation of GST from the amorphous phase to the metastable rock salt (RS) phase and further crystallization into the hexagonal (HEX) phase. These results align with the findings from the variable-temperature resistance experiments, demonstrating that N doping inhibits the phase transformation of GST. To verify the superior heat-resistant properties of N-GST, constant-temperature resistance failure tests were separately conducted on both GST and N-GST. The failure time





**FIG. 1.** (a) The synthesis process of the multi-layer emitter. (b) The concept of camouflage and thermal management for MIR compatibility. The surface of the car is covered with the designed membrane structure. They are hidden in the visible camera and infrared camera, and integrated into the environment.



**FIG. 2.** (a) Temperature dependence from the resistance of the amorphous GST films with the same heating rate of 10  $^{\circ}\text{C}/\text{min}$  at four kinds of N concentration. (b) Temperature-dependent Raman spectra of N-GST in the frequency range of 50–300  $\text{cm}^{-1}$ . The XPS spectra of (c) Ge 3d, (d) Sb 3d, and (e) Te 3d in N-GST, respectively. (f) The XRD patterns of the amorphous and the crystalline N-GST films, respectively.

was defined as the moment when the resistance value of the thin film material drops to 50% of its initial value at a specific temperature. As shown in Figs. S2(a) and S2(b), thin film samples underwent constant-temperature resistance testing at various temperature points to determine the material's failure time under different conditions. The temperature–failure time curves, fitted based on the Arrhenius equation<sup>64</sup> [Fig. S2(c)], indicate that while GST endures roughly 4.5 days at 100 °C, N-GST can withstand as long as 9.2 years. Therefore, compared with GST, the heat resistance and applicability of N-GST are significantly improved in the thermal stealth.

The detailed investigation of the chemical composition and electronic valence of the N-GST film was carried out using x-ray photoelectron spectroscopy (XPS). The spectra were uniformly calibrated based on the C 1s emission at 284.6 eV. Figure 2(c) presents the deconvolution of the Ge 3d spectrum, revealing three distinct chemical states: Ge<sup>0</sup>, Ge–N (Ge<sub>3</sub>N<sub>4</sub>), and Ge–Te, with peaks at 30.46, 31.33, and 32.12 eV, respectively. In Fig. 2(d), the Sb 3d orbital shows peaks at 528.93 and 538.32 eV, attributed to the Sb<sub>5/2</sub> and Sb<sub>3/2</sub>, while the peak at 531.04 eV is associated with the Sb–N bond. As for the Te 3d spectra in Fig. 2(e), only the peaks of the Te–Te bond at 571.9 and 583.4 eV are highlighted. The relatively small Ge–N peak detected in comparison to the XPS plot of GST (as shown in Fig. S3) is due to the formation of a minor amount of nitride in GST during the nitrogen doping process. In Fig. 2(f), the XRD plots compare the amorphous and crystalline states of N-GST after annealing at 230 °C. The amorphous state of GST shows almost no peaks in the XRD, whereas well-defined peaks at 29.63°, 43.03°, and 54.23° represent the (200), (220), and (222) facets of crystalline GST (JCPDS54-0484). A weak diffraction peak associated with nitride was observed at 38.35°.<sup>66</sup> It is likely that a small portion of the doped N is bonded to Ge or Sb, potentially more stably embedded in the crystal structure at vacant or interstitial sites, contributing to improved thermal stability. Additionally, the phase change can be distinguished by alterations in the optical image. As shown in Fig. S4, spectral transmittance measurements conducted for both amorphous and crystalline N-GST reveal significant differences in the transmission spectra between the two states. This is due to the atomic rearrangement occurring at the phase change temperature, resulting in alterations in optical properties. The corresponding optical band gaps, calculated as displayed in Fig. S5, are 0.97 and 0.52 eV, respectively. This demonstrates an increased bandgap between the amorphous and crystalline states, contributing to enhanced thermal stability.

To explore the infrared stealth properties of N-GST films, we initially investigated the dependence of the infrared emissivity of the N-GST/Au emitter on their internal structure using FDTD simulation software simulations. The simulated emitter comprises an Au back-reflector and a certain thickness of N-GST. The thickness of Au is determined to be 100 nm based on its high infrared reflectivity and cost considerations (Fig. S6). In the simulation, the relative permittivity of Au, derived from Olmon's work, positions it as a highly reflective material in the MIR band, effectively reflecting almost 100% of the incident wave. While other metals like Al and Ag exhibit similar properties, their stability falls short compared to Au, making it the more preferred choice for this application. The relative permittivity of N-GST (Fig. S7) was determined using spectroscopic ellipsometry (SE). The measured dielectric constants reveal a near-zero extinction coefficient in the amorphous phase [N-GST(a)], while the extinction coefficient of the crystalline phase [N-GST(c)] increases with longer

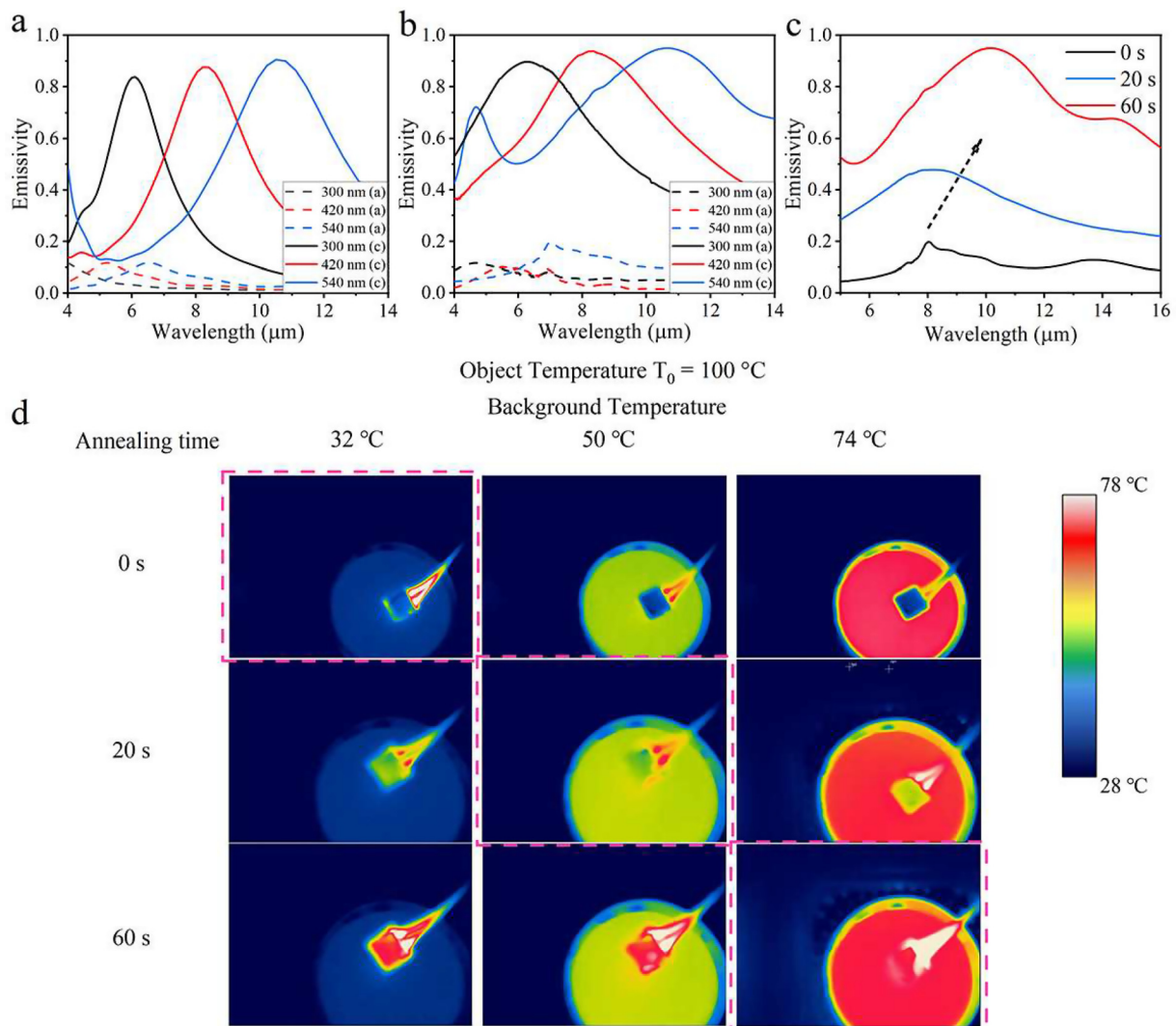
wavelengths. This difference is due to the change in electronic states during the rapid crystallization from amorphous GST to the RS phase.<sup>67</sup> The amorphous phase of PCM typically follows the 8-N covalent bonding rule for the coordination numbers, a principle observed by Kolobov *et al.*<sup>68</sup> and Baker *et al.*<sup>69</sup> The crystal structures of PCM are based on distorted cubic structures, characterized by a unique electron configuration known as resonance bonding, a concept introduced by Pauling.<sup>70</sup> Resonance bonding involves atoms with half-filled *p*-orbitals forming longer range order bonds, leading to increased electron delocalization and higher electronic polarizability.<sup>71,72</sup> The transition between amorphous and crystalline phases involves a substantial rearrangement of nearby neighbors, resulting in a considerable contrast in optical constants between the two structural phases. This transition can be attributed to a bonding change, resulting in a significant change in the optical properties of the material.

Figure 3(a) depicts the emissivity under normal incidence, analyzed using the finite-difference time-domain (FDTD) method. According to Kirchhoff's law of thermal emission, the emissivity of an object at thermal equilibrium equals its absorptivity. Thus, the emissivity ( $\epsilon$ ) of an opaque object is defined as  $\epsilon = 1 - Ref$ , where  $Ref$  represents the reflectivity. In the N-GST(a)/Au sample, minimal resistive loss occurs in the N-GST(a) layer. The observed absorption is primarily due to the resistive losses in the Au layer because the metal film is not an ideal total reflector. However, in the N-GST(c)/Au sample, featuring a larger extinction coefficient, the higher resistive loss leads to greater absorption. Both samples display significant contrast in terms of infrared emissivity. Furthermore, the planar cavity formed by N-GST on the Au reflective layer resonantly absorbs specific wavelengths, a crucial factor contributing to high emissivity. The incident light undergoes multiple reflections at the interface of film–air and film–mirror, and the interference causes cavity effect, which leads to enhanced absorption. With a fixed thickness, at a specific wavelength, multiple reflections of light waves form peak signals, while at other wavelengths they cancel each other out.<sup>73</sup> As the thickness of the film increases, the interference path length also increases, resulting in an increased phase shift. This typically causes longer wavelength light to be selectively amplified, resulting in a redshift phenomenon. This illustrates its potential as a wavelength-selective thermal emitter. The emission spectra, obtained from the infrared reflectance measured by Fourier transform infrared spectroscopy [Fig. 3(b)], exhibit good agreement with the simulation results. The slight light scattering comes from the complex atomic vibration caused by doping. Standard infrared cameras, including the one used in this study, can detect infrared spectra within the 7.5–13  $\mu\text{m}$  range. Notably, the peak emissivity of the 540 nm thick N-GST is centered at 10.5  $\mu\text{m}$ , aligning closely with the detection range's center. This positioning allows for maximum contrast in the emitter's infrared emission intensity between its crystalline and amorphous states, offering potential for a broad range of camouflage temperatures.

The difference in dielectric constant between N-GST(a) and N-GST(c) is primarily due to their distinct atomic distributions. N-GST (a) can undergo thermal annealing for different durations to achieve intermediate states presenting varying degrees of crystallization [N-GST(i)]. N-GST(i) maintains a specific ratio of N-GST(a) to N-GST (c), resulting in its emissivity falling between these two states. This brief annealing process occurred within a small, enclosed cavity heated precisely to 230 °C in a nitrogen atmosphere. Figure 3(c) demonstrates

that as the annealing time increases from 0 to 60 s, the infrared emissivity of the structure gradually rises. This characteristic allows objects at a constant temperature to match the radiative temperature of the background in an infrared camera, seamlessly blending with the surroundings. The practical result is shown in Fig. 3(d), where the emissivity of the variable-temperature blackbody is 0.96, which is close to most natural environments, such as soil ( $\epsilon = 0.91$ ), grass ( $\epsilon = 0.95$ ), and shrubs ( $\epsilon = 0.98$ ). Hence, it is suitable for simulating diverse background temperatures. An infrared camera was employed to capture the image, demonstrating the effective camouflage capacity of the system. At an object temperature of 100 °C, both the N-GST(a)/Au and the background registered a radiative temperature of 32 °C, rendering

them indistinguishable in the infrared camera. However, when the background temperature increased to 50 °C, N-GST(a)/Au stood out due to the variance in radiative temperature. After 20 s of annealing, N-GST(i) matched the background temperature, and following 60 s of annealing, the object concealed within the background at 74 °C. Notably, in comparison to GST, N-doped GST displays superior heat resistance. When both GST and N-GST were exposed to a 100 °C hot plate, GST quickly increased its radiation temperature, almost completing its phase transition in around 130 h. Conversely, N-GST consistently maintained a lower radiation temperature, showcasing its significantly improved heat resistance (Fig. S8).



**FIG. 3.** (a) Simulated and (b) experimental normal-incidence emissivity of the N-GST/Au(a) and N-GST/Au(c) samples in the MIR with three different N-GST thicknesses of 300, 420, and 540 nm, respectively. The dashed and solid lines are for the N-GST/Au(a) and N-GST/Au(c) samples, respectively. Note that (a) and (c) denote the N-GST/Au(a) and N-GST/Au(c) samples, respectively. (c) The measured emissivity is collected after different annealing times at a normal angle for N-GST/Au(a) and N-GST/Au(c) devices. The object is annealed at 230 °C for 0, 20, and 60 s in order to obtain different N-GST crystallization fractions. (d) Infrared images recorded at different background temperatures at different background temperatures (32, 50, and 74 °C) and a fixed object temperature (100 °C), respectively.

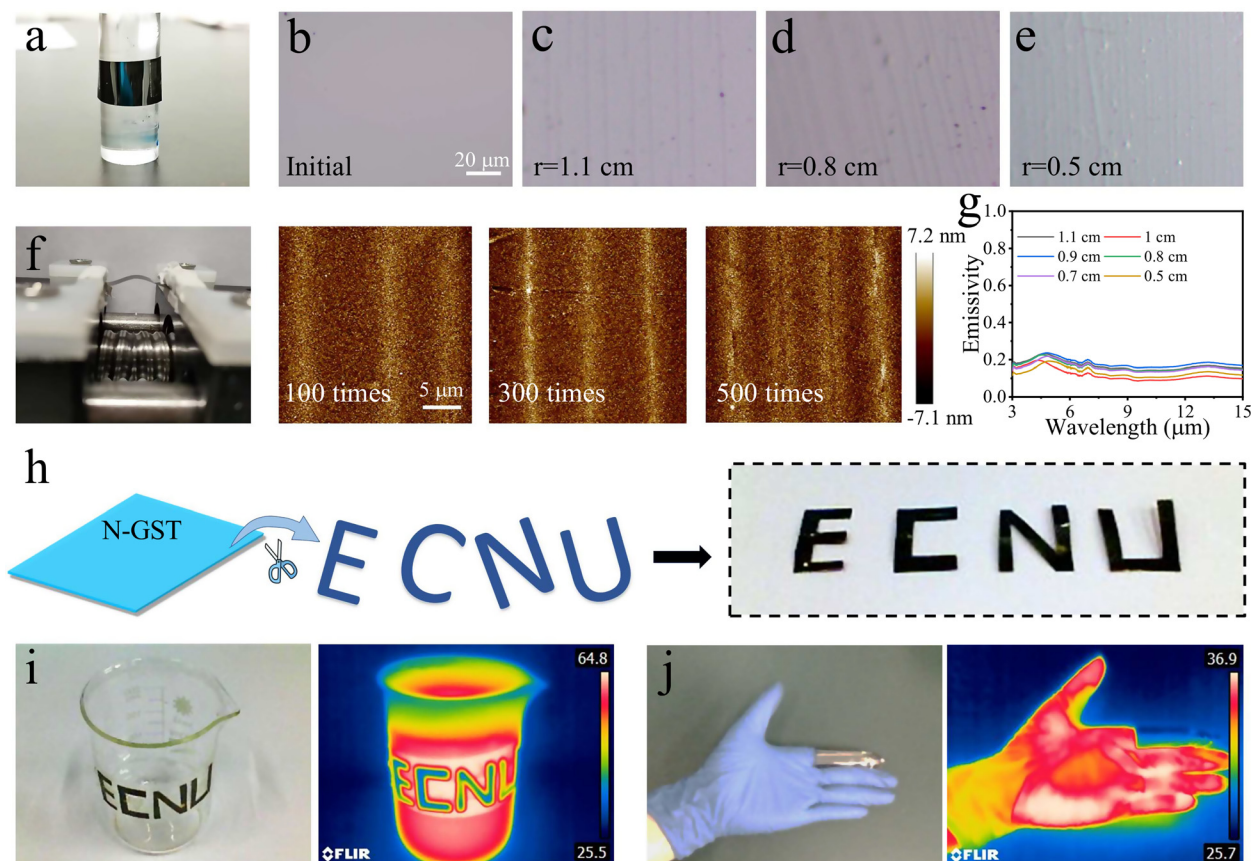


To demonstrate the practical application of dynamically controllable emissivity in infrared camouflage, a thermally guided emissivity dynamic control device was developed. Illustrated in Fig. S9, it comprised an indium tin oxide (ITO) line (thickness: 100 nm) serving as a heater, flanked by silver electrodes (thickness: 200 nm) connected with wires. Above this assembly lay silicon dioxide, acting as an electrical isolation layer, and the N-GST/Au emitter. A heat stage with a surface temperature of 100 °C was selected as the target for camouflaging. The process, recorded in a video provided in the [supplementary material](#), involved controlling the emissivity using an ITO heater. An infrared camera monitored the target. When the applied voltage was set to zero, the upper part, covered by the thermal emitter, exhibited a lower radiation temperature (blue). Applying 80 V caused the N-GST/Au emitter to rapidly reach around 230 °C via the ITO heater. After approximately 20 s, the N-GST/Au emitter cooled down, showing a different radiation temperature (yellow). Reapplying voltage led to higher thermal emissions (red). Hence, emissivity could be dynamically controlled by adjusting the voltage application time.

To verify the robustness of thermal camouflage, we further evaluated the thermal emission of the camouflage device at observation angles from 0° to 60°. In Fig. S10(a), as the observation angle extended

from 0° to 60°, the recorded thermal temperature of the object remained consistent with the background, showcasing the sustained effectiveness of the thermal camouflage device even at wide observation angles. The thermal emission for both transverse electric (TE) [Figs. S10(b) and S10(e)] and transverse magnetic (TM) [Figs. S10(c) and S10(f)] polarizations for N-GST/Au(a) and N-GST/Au(c) devices was also calculated. The average emissivities of TM and TE polarizations [Figs. S10(d) and S10(g)] indicate that the observation angles (0°–60°) have minimal impact on the emissivities, suggesting practical applications.

When the thickness of gold is sufficient, N-GST/Au emitters have lower substrate requirements, favoring the preparation of flexible infrared phase change camouflage material. The intermediate Cr layer enhances the adhesion between the Au layer and the substrate. In the further work, the silicon substrate was replaced with a polyimide (PI) film, 0.125 mm thick, to enhance flexibility. Bending tests were employed to evaluate the N-GST/Au emitter's flexibility. [Figure 4\(a\)](#) presents a photograph of the bending sample. [Figure 4\(b\)](#) displays an optical microscope image of the emitter surface before bending, exhibiting an impressively smooth



**FIG. 4.** (a) Image of bent samples. (b)–(e) Optical microscopy images captured during the bending of sample surfaces. (f) Cyclic bending test device and AFM images of sample surfaces after various bending times. (g) Emissivity of N-GST emitter/PI after various degrees of bending. (h) Digital images of “ECNU” letters cut from the emitter/PI directly. (i) Thermal images of a beaker filled with boiling water covered by “ECNU” letters. (j) Thermal camouflage effect of finger wrapped in emitter/PI.

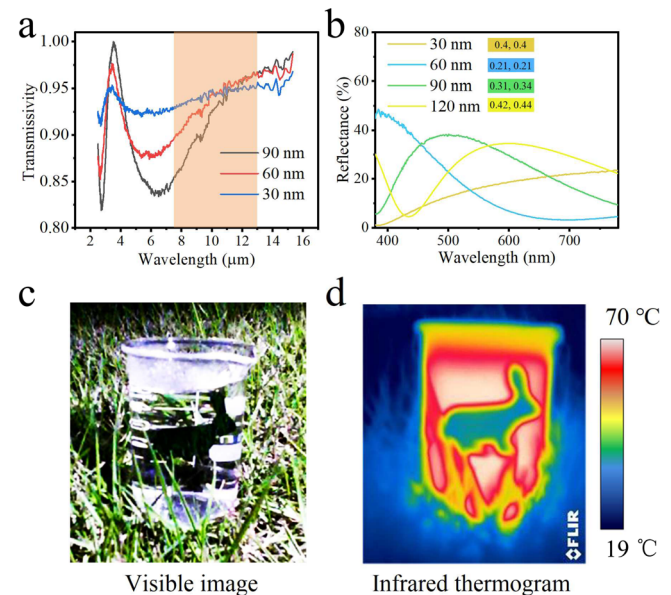


film. Optical images in Figs. 4(c) and 4(e) depict the emitter in bent states. Since N-GST is a brittle material, when the emitter is bent to a radius of curvature of 1.1 cm, the film is cracked by the bending force [Fig. 4(c)], which is perpendicular to the stress direction. Reducing the curvature radius to 0.5 cm led to smaller spacing between cracks but a larger crack width. Figure 4(g) displays the infrared emission spectra of N-GST after varying degrees of bending in the released state, consistently maintaining low and nearly identical levels. The maximum average crack width, about 600 nm, was significantly smaller than the infrared camera's resolution. The PI covered by N-GST/Au was fixed to a curved Al sheet for convenient observation via an infrared thermal imager. Clearly, the three different phases of N-GST exhibited similar radiation temperatures before and after bending (Fig. S11). Infrared images in Fig. S12 also revealed that bending did not significantly impact the emitter's infrared emission intensity. Additionally, cyclic bending experiments were conducted on the emitter [device as shown in Fig. 4(f)]. For a more detailed inspection, the AFM technique was used to capture images of the PI after hundreds of repeated bendings (radius of 1 cm). The experimental results show that the crack density gradually increased with cycles. This is because different stress concentration points appear in the material under cyclic loading, leading to the formation and propagation of new cracks.<sup>74</sup> Yet, the corresponding emission intensity, recorded with the infrared camera (Fig. S13), exhibited no significant change. Furthermore, a temperature-dependent resistance test was carried out on the curved film to explore the impact of crack testing on thin film phase transition temperatures. Interestingly, there was no noticeable difference in the film's phase transition temperature before and after bending (Fig. S14).

It needs to be noted that after small-radius compression or multiple bending, N-GST films remain firmly attached to the substrate without any material delamination. First, the Au/Cr film layer possesses excellent toughness, enhancing the adhesion between N-GST and the substrate, with minimal impact on the strain induced within N-GST. Second, according to the expression for the strain in bending of a thin film deposited on a flexible substrate  $\epsilon_f = \left(\frac{d_f + d_s}{2r}\right) \left(\frac{1 + 2\eta + \chi\eta^2}{(1 + \eta)(1 + \chi\eta)}\right)$ ,<sup>75,76</sup> where  $d_f$  and  $d_s$  denote the thicknesses of the film and substrate, respectively;  $\eta = d_f/d_s$ ;  $r$  is the radius of curvature;  $\chi = Y_f/Y_s$  where  $Y_f$  and  $Y_s$  denote the Young's modulus of the film and the substrate. The Young's modulus of the N-GST is 32 GPa, which is given by the load-displacement curve obtained by the sub-micron indentation technique (Fig. S15). Considering Young's modulus of PI of 2.5–4 GPa, the strain induced by  $r = 0.5$  cm in the N-GST film was calculated to be 1.19%–1.22%, which can be mitigated by forming cracks to reduce the effect of the bending strain. As a result, the N-GST/Au emitter has excellent flexibility and can be cut into different shapes. The letters "ECNU" cut from the flexible emitter can be clearly shown in Fig. 4(h). Then the cut letters are affixed to the wall of a beaker filled with boiling water, displaying a notable contrast in emission intensity compared to the background, owing to the low emissivity as observed by a thermal imaging camera [Fig. 4(i)]. To further demonstrate its utility, the emitter was made into a finger cover, as shown in Fig. 4(j), where the covered finger almost blends in with the background, revealing the stealth capability of the flexible emitter in various scenarios.

Adapting to diverse detection methods across different spectral ranges, stacking multilayer membranes becomes a potent strategy to enhance camouflage technology. ZnS, when placed atop the N-GST, facilitates spectral compatibility due to wavelength discrepancies. This

is because ZnS is a typical infrared transparent material, and changing the thickness of ZnS hardly affects the emission in the infrared region.<sup>77</sup> So, the N-GST emitter and ZnS film can independently modulate the infrared and visible light bands, respectively. As depicted in Fig. 5(a), ZnS, a standard infrared transparent material, consistently transmits above 85% within most infrared camera detection ranges. Known for its optical properties, the reflection in the visible range can be modulated by altering the film's thickness. Figure 5(b) displays the reflection spectra in the visible range for ZnS films of varying thicknesses, showcasing different anti-reflection peaks. The chromaticity coordinates ( $x$ ,  $y$ ) for each reflection spectrum, calculated using CIE-1931 chromaticity coordinates, are described in the figure's legend. Practical applications allow simulating different background colors by regulating the thickness of the top ZnS layer—30 nm for yellow sand, 60 nm for the sky and ocean, 90 nm for grassy green hills, and so forth. Manipulating the top ZnS layer's thickness can simulate various background colors. Figure 5(c) exhibits an example where 90 nm of ZnS was deposited on a flexible N-GST emitter, crafted into a rabbit pattern. The rabbit, placed in hot water within a beaker, simulates the camouflage device's stealth effect on a heated object. Camera images portray the rabbit as inconspicuous, mirroring the grass's color, demonstrating its seamless integration into the background. In the captured thermal image, the segment covered by the rabbit exhibits a light blue hue, resembling the weak thermal radiation emitted by the bare background. This showcases the device's adeptness in merging into the background seamlessly, visible in both light and infrared detection, underscoring the efficacy of the composite multilayer structure for multispectral concealment. Compared to previously reported phase change material emitters (Table I), the ZnS/N-GST multilayer structure exhibits significantly improved operating temperatures. Furthermore, our modulation performance (emissivity change) can



**FIG. 5.** (a) Infrared transmittance and (b) visible light reflection spectrum of ZnS film with different thicknesses. (c) Visual effect and (d) infrared thermogram of beaker filled with boiling water covered with ZnS/N-GST emitter/PI.

TABLE I. Comparison of stealth performances for ZnS/N-GST with the reported thermal emitter.

Materials	Structure	Working bands	Working temperature	Emissivity changes	Reference
			(°C)	$\Delta \varepsilon$	
GST/Au	Coatings	8–14 $\mu\text{m}$	< 150	0.15–0.65 ( $\Delta \varepsilon = 0.5$ )	78
$\text{W}_x\text{V}_{1-x}\text{O}_2$	Metasurface	8–13 $\mu\text{m}$	< 22	0.2–0.9 ( $\Delta \varepsilon = 0.7$ )	79
$\text{VO}_x/\text{SiO}_x/\text{Au}/\text{Su8u}$	Metamaterial	3–5 and 8–12 $\mu\text{m}$	< 67	$\Delta \varepsilon = 0.45$	80
GST/ $\text{VO}_2\text{S}/\text{Ag}$	Coatings	5–14 $\mu\text{m}$	< 67	0.02–0.19 ( $\Delta \varepsilon = 0.17$ )	81
GST/ $\text{VO}_2\text{S}/\text{Au}$	Coatings	3–5 and 8–14 $\mu\text{m}$	< 67	$\Delta \varepsilon_{8-14\mu\text{m}} = 0.25$	82
$\text{SmNiO}_3$	Coating	8–14 $\mu\text{m}$	< 140	0.28–0.55 ( $\Delta \varepsilon = 0.27$ )	17
$\text{Sb}_2\text{S}_3/\text{GST}/\text{VO}_2$	Metasurface	2–8 $\mu\text{m}$	< 67	$\Delta \varepsilon = 0.45$	83
<b>ZnS/N-Ge<sub>2</sub>Sb<sub>2</sub>Te<sub>5</sub></b>	Coatings	380–780 nm and 8–14 $\mu\text{m}$	< 210	0.13–0.83 ( $\Delta \varepsilon = 0.7$ )	<b>This work</b>

compete with the single-band modulation performance reported in previous studies. Unlike most single- or dual-band modulation in the IR spectrum, the integration of visible light camouflage and infrared dynamic modulation is achieved in our device. This encourages further exploration in the future.

#### IV. CONCLUSION AND OUTLOOK

In conclusion, the GST modified by N doping was studied, and the N-GST thin film is still nonvolatile, and its phase transition temperature is about 60 °C higher than that of GST. The thermal emitter composed of N-GST and an Au film can achieve wide wavelength selectivity by controlling the thickness of the N-GST layer. When N-GST is transformed between crystalline and amorphous states, the radiation of the target at a fixed temperature can be dynamically controlled to match different background temperatures. In addition, although N-GST is a brittle material, the demonstrated emitter shows good bending resistance and can be flexibly applied to the surface of the target. In order to meet the new applications of multi-spectral camouflage, we also designed a multi-layer membrane structure to realize dual-band camouflage. These devices based on N-GST provide a new strategy for accomplishing high-temperature thermal camouflage and multi-spectral camouflage based on phase change materials with a dynamic modulation function.

#### SUPPLEMENTARY MATERIAL

See the [supplementary material](#) for details on the influence of nitrogen/argon flow ratios on the atomic ratio of N-GST, temperature resistance analysis, optical characteristics of N-GST, the dynamic control device of thermal conduction emissivity, robustness analysis of the observation angle, and the bending stability of the device.

#### ACKNOWLEDGMENTS

L. Huo is grateful to Dr. Ming Li for the technique assistance. The authors gratefully acknowledge the support of the National Natural Science Foundation of China (Grant Nos. 62375086 and 62090013), the National Key Research and Development Program of China (Grant No. 2019YFB2203403), the Project of Science and Technology Commission of Shanghai Municipality (Grant No. 21JC1402100), and the Program for Professor of Special Appointment (Eastern Scholar) at Shanghai Institutions of Higher Learning.

#### AUTHOR DECLARATIONS

##### Conflict of Interest

The authors have no conflicts to disclose.

##### Author Contributions

**Liuxiang Huo:** Conceptualization (lead); Data curation (lead); Formal analysis (lead); Writing – original draft (lead). **Lin Wang:** Formal analysis (supporting); Investigation (supporting). **Shubing Li:** Formal analysis (supporting). **Xionghu Xu:** Formal analysis (supporting); Methodology (supporting). **Liangqing Zhu:** Formal analysis (supporting); Investigation (supporting). **Yawei Li:** Data curation (supporting). **Liyang Shang:** Formal analysis (supporting). **Kai Jiang:** Formal analysis (supporting). **Junhao Chu:** Supervision (equal). **Zhigao Hu:** Conceptualization (equal); Project administration (lead); Supervision (lead); Writing – review & editing (lead).

#### DATA AVAILABILITY

The data that support the findings of this study are available from the corresponding author upon reasonable request.

#### REFERENCES

- J. Teyssier, S. V. Saenko, D. Marel, and M. C. Milinkovitch, *Nat. Commun.* **6**, 6368 (2015).
- C. Xu, G. T. Stiubianu, and A. A. Gorodetsky, *Science* **359**, 1495 (2018).
- L. Phan, W. G. Walkup, D. D. Ordinario, E. Karshalev, J.-M. Jocson, A. M. Burke, and A. A. Gorodetsky, *Adv. Mater.* **25**, 5621 (2013).
- B. Wang, Y. Huang, Y. Han, W. Zhang, C. Zhou, Q. Jiang, F. Chen, X. Wu, R. Li, P. Lyu, S. Zhao, F. Wang, and R. Zhang, *Nano Lett.* **22**, 3713 (2022).
- R. Fleury and A. Alu, *Prog. Electromagn. Res.* **147**, 171 (2014).
- S. Dang, Z. Wang, and H. Ye, *Mater. Res. Express* **6**, 106422 (2019).
- Y. Li, X. Bai, T. Yang, H. Luo, and C.-W. Qiu, *Nat. Commun.* **9**, 273 (2018).
- S. Hong, S. Shin, and R. Chen, *Adv. Funct. Mater.* **30**, 1909788 (2020).
- F. Lang, H. Wang, S. Zhang, J. Liu, and H. Yan, *Int. J. Thermophys.* **39**, 6 (2018).
- C. Yu, Y. Li, X. Zhang, X. Huang, V. Malyarchuk, S. Wang, Y. Shi, L. Gao, Y. Su, Y. Zhang, H. Xu, R. T. Hanlon, Y. Huang, and J. A. Rogers, *Proc. Natl. Acad. Sci. U. S. A.* **111**, 12998 (2014).
- H. Liu, C. Wang, G. Chen, Y. Liao, M. Mao, T. Cheng, A. Libanori, X. Xiao, H. Hu, K. Liu, and J. Chen, *Nano Energy* **93**, 106855 (2022).
- D. Franklin, S. Modak, A. V. Guardado, A. Safaei, and D. Chanda, *Light Sci. Appl.* **7**, 93 (2018).
- H. K. Woo, K. Zhou, S.-K. Kim, A. Manjarrez, M. J. Hoque, T.-Y. Seong, and L. Cai, *Adv. Funct. Mater.* **32**, 2201432 (2022).

- <sup>14</sup>R. Hu, W. Xi, Y. D. Liu, K. C. Tang, J. L. Song, X. B. Luo, J. Q. Wu, and C.-W. Qiu, *Mater. Today* **45**, 120 (2021).
- <sup>15</sup>J. Lyu, Z. Liu, X. Wu, G. Li, D. Fang, and X. Zhang, *ACS Nano* **13**, 2236 (2019).
- <sup>16</sup>O. Salihoglu, H. B. Uzlu, O. Yakar, S. Aas, O. Balci, N. Kakenov, S. Balci, S. Olcum, S. Suzer, and C. Kocabas, *Nano Lett.* **18**, 4541 (2018).
- <sup>17</sup>A. Shahsafi, P. Roney, Y. Zhou, Z. Zhang, Y. Xiao, C. Wan, R. Wambold, J. Salman, Z. Yu, J. Li, J. T. Sadowski, R. Comin, S. Ramanathan, and M. A. Kats, *Proc. Natl. Acad. Sci. U. S. A.* **116**, 26402 (2019).
- <sup>18</sup>S. Chandra, D. Franklin, J. Cozart, A. Safaei, and D. Chanda, *ACS Photonics* **5**, 4513 (2018).
- <sup>19</sup>L. Zhao, R. Zhang, C. Deng, Y. Peng, and T. Jiang, *Nanomaterials* **9**, 1096 (2019).
- <sup>20</sup>H. Ji, D. Liu, H. Cheng, C. Zhang, and L. Yang, *Sol. Energy Mater. Sol. Cells* **175**, 96 (2018).
- <sup>21</sup>G. Cui, Z. Peng, X. Chen, Y. Cheng, L. Lu, S. Cao, S. Ji, G. Qu, L. Zhao, S. Wang, S. Wang, Y. Li, H. Ci, M. Li, and Z. Liu, *Adv. Sci.* **9**, 2105004 (2022).
- <sup>22</sup>M. S. Ergoktas, G. Bakan, P. Steiner, C. Bartlam, Y. Malevich, E. O. Yenigun, G. He, N. Karim, P. Cataldi, M. A. Bissett, I. A. Kinloch, K. S. Novoselov, and C. Kocabas, *Nano Lett.* **20**, 5346 (2020).
- <sup>23</sup>T. Cui, K. Yip, A. Hassan, G. Wang, X. Liu, Y. Sun, and T. Filleter, *Sci Adv.* **6**, eabb1335 (2020).
- <sup>24</sup>Z. Li, X. Chao, A. Balilonda, and W. Chen, *InfoMat* **5**, e12418 (2023).
- <sup>25</sup>Z. Xu, Q. Li, K. Du, S. Long, Y. Yang, X. Cao, H. Luo, H. Zhu, P. Ghosh, W. Shen, and M. Qiu, *Laser Photonics Rev.* **14**, 1900162 (2020).
- <sup>26</sup>Z. J. Coppens and J. G. Valentine, *Adv. Mater.* **29**, 1701275 (2017).
- <sup>27</sup>M. Li, S. Li, M. Deng, X. Xu, K. Dai, A. Cui, X. Zhou, K. Jiang, L. Shang, Y. Li, J. Zhang, L. Zhu, J. Chu, and Z. Hu, *J. Appl. Phys.* **133**, 053101 (2023).
- <sup>28</sup>L. Zhang, R. F. Waters, K. F. MacDonald, and N. I. Zheludev, *Appl. Phys. Rev.* **8**, 011404 (2021).
- <sup>29</sup>M. Thomaschewski and S. I. Bozhevolnyi, *Appl. Phys. Rev.* **9**, 021311 (2022).
- <sup>30</sup>E. M. Vinod, R. Naik, A. P. A. Faiyas, R. Ganesan, and K. S. Sangunni, *J. Non-Cryst. Solids* **356**, 2172–2174 (2010).
- <sup>31</sup>E. M. Vinod, R. Naik, R. Ganesan, and K. S. Sangunni, *J. Non-Cryst. Solids* **358**, 2927–2930 (2012).
- <sup>32</sup>D. Sahoo and R. Naik, *Mater. Res. Bull.* **148**, 111679 (2022).
- <sup>33</sup>Y. Zhu, Z. Zhang, S. Song, H. Xie, Z. Song, X. Li, L. Shen, L. Li, L. Wu, and B. Liu, *Mater. Res. Bull.* **64**, 333–336 (2015).
- <sup>34</sup>Q. Gao and L. Chen, *Appl. Phys. A* **125**, 564 (2019).
- <sup>35</sup>V. E. Madhavan, M. Carignano, A. Kachmar, and K. S. Sangunni, *Sci. Rep.* **9**, 12985 (2019).
- <sup>36</sup>Y. Qu, Q. Li, L. Cai, M. Pan, P. Ghosh, K. Du, and M. Qiu, *Light Sci. Appl.* **7**, 26 (2018).
- <sup>37</sup>C. Kim, Y. Kim, and M. Lee, *Adv. Mater. Technol.* **7**, 2101349 (2022).
- <sup>38</sup>Z. Xu, H. Luo, H. Zhu, Y. Hong, W. Shen, J. Ding, S. Kaur, P. Ghosh, M. Qiu, and Q. Li, *Nano Lett.* **21**, 5269 (2021).
- <sup>39</sup>L. Li, M. Shi, X. Liu, X. Jin, Y. Cao, Y. Yang, and W. Wang, *Adv. Funct. Mater.* **31**, 2101381 (2021).
- <sup>40</sup>M. Rude, R. E. Simpson, R. Quidant, V. Pruneri, and J. Renger, *ACS Photonics* **2**, 669 (2015).
- <sup>41</sup>X.-F. Liu, J.-F. He, Y.-G. Li, H. Li, W. Lei, Q.-L. Jia, S.-W. Zhang, and H.-J. Zhang, *Rare Met.* **42**, 3829–3838 (2023).
- <sup>42</sup>X. Liao, M. Yan, and L. Mai, *Matter* **6**, 2602–2604 (2023).
- <sup>43</sup>M. Gerken, J. Fritze, M. Münzberg, and M. Weispfenning, *Proc. SPIE* **10177**, 101770C (2017).
- <sup>44</sup>N. Kumar and A. Dixit, *Nanotechnology for Defence Applications* (Springer International Publishing, 2019).
- <sup>45</sup>L. Yao, L. Pan, S. Zhou, H. Liu, H. Mei, Y. Li, K. G. Dassios, P. Colombo, L. Cheng, and L. Zhang, *Mater. Horiz.* **10**, 3404 (2023).
- <sup>46</sup>Y. Peng, Y. Ye, Z. Huang, Y. Ma, J. Tang, J. Zhou, L. C. Greenburg, Y. Cui, L. Fan, W. Jin, S. Fan, S. Zhai, A. Majumdar, and X. Luo, *Nat. Sustain.* **5**, 339 (2022).
- <sup>47</sup>M. Li, D. Liu, H. Cheng, L. Peng, and M. Zu, *Sci. Adv.* **6**, eaba3494 (2020).
- <sup>48</sup>M. S. Ergoktas, G. Bakan, E. Kovalska, L. W. L. Fevre, R. P. Fields, P. Steiner, X. Yu, O. Salihoglu, S. Balci, V. I. Fal'ko, K. Novoselov, R. A. W. Dryfe, and C. Kocabas, *Nat. Photonics* **15**, 493 (2021).
- <sup>49</sup>E. Buhara, A. Ghobadi, and E. Ozbay, *Opt. Lett.* **46**, 4777 (2021).
- <sup>50</sup>D. Qi, F. Chen, X. Wang, H. Luo, Y. Cheng, X. Niu, and R. Gong, *Opt. Lett.* **43**, 5323 (2018).
- <sup>51</sup>N. Lee, J.-S. Lim, I. Chang, H. M. Bae, J. Nam, and H. H. Cho, *Adv. Opt. Mater.* **10**, 2200448 (2022).
- <sup>52</sup>M. Qin, L. Zhang, X. Zhao, and H. Wu, *Adv. Funct. Mater.* **31**, 2103436 (2021).
- <sup>53</sup>L. Peng, D. Liu, H. Cheng, S. Zhou, and M. Zu, *Adv. Opt. Mater.* **6**, 1801006 (2018).
- <sup>54</sup>N. Lee, T. Kim, J.-S. Lim, I. Chang, and H. H. Cho, *ACS Appl. Mater. Interfaces* **11**, 21250 (2019).
- <sup>55</sup>T. Kim, J. Y. Bae, N. Lee, and H. H. Cho, *Adv. Funct. Mater.* **29**, 1807319 (2019).
- <sup>56</sup>M. Zhang, M. Pu, F. Zhang, Y. Guo, Q. He, X. Ma, Y. Huang, X. Li, H. Yu, and X. Luo, *Adv. Sci.* **5**, 1800835 (2018).
- <sup>57</sup>H. Zhu, Q. Li, C. Zheng, Y. Hong, Z. Xu, H. Wang, W. Shen, S. Kaur, P. Ghosh, and M. Qiu, *Light Sci. Appl.* **9**, 60 (2020).
- <sup>58</sup>X. Feng, M. Pu, F. Zhang, R. Pan, S. Wang, J. Gong, R. Zhang, Y. Guo, X. Li, X. Ma, and X. Luo, *Adv. Funct. Mater.* **32**, 2205547 (2022).
- <sup>59</sup>L. Yuan, C. Huang, J. Liao, C. Ji, J. Huang, Y. Wang, and X. Luo, *Adv. Sci.* **9**, 2201054 (2022).
- <sup>60</sup>Y. Huang, Y. Zhu, B. Qin, Y. Zhou, R. Qin, P. Ghosh, M. Qiu, and Q. Li, *Nanophotonics* **11**, 3613 (2022).
- <sup>61</sup>R. L. Olmon, B. Slovick, T. W. Johnson, D. Shelton, S.-H. Oh, G. D. Boreman, and M. B. Raschke, *Phys. Rev. B* **86**, 235147 (2012).
- <sup>62</sup>A. V. Kolobov, P. Fons, B. Hyot, B. André, Y. Tominaga, H. Tamenori, K. Yoshikawa, and J. Kobayashi, *Appl. Phys. Lett.* **100**, 061910 (2012).
- <sup>63</sup>S. Guo, Z. G. Hu, X. L. Ji, T. Huang, X. L. Zhang, L. C. Wu, Z. T. Song, and J. H. Chu, *RSC Adv.* **4**, 57218 (2014).
- <sup>64</sup>K. S. Andrikopoulou, S. N. Yannopoulos, G. A. Voyiatzis, A. V. Kolobov, M. Ribes, and J. Tominaga, *J. Phys.: Condens. Matter* **18**, 965 (2006).
- <sup>65</sup>M. Li, M. Xie, H. Ji, J. Zhou, K. Jiang, L. Shang, Y. Li, Z. Hu, and J. Chu, *Appl. Phys. Lett.* **116**, 162102 (2020).
- <sup>66</sup>D. Qian, J. Miao, P. Yuan, D. Song, and R. Lan, *J. Mater. Sci.: Mater. Electron.* **33**, 12750 (2022).
- <sup>67</sup>V. Bragaglia, F. Arciprete, W. Zhang, A. M. Mio, E. Zallo, K. Perumal, A. Giussani, S. Cecchi, J. E. Boschker, H. Riechert, S. Privitera, E. Rimini, R. Mazzarello, and R. Calarco, *Sci. Rep.* **6**, 23843 (2016).
- <sup>68</sup>A. V. Kolobov, P. Fons, A. I. Frenkel, A. L. Ankudinov, J. Tominaga, and T. Uruga, *Nat. Mater.* **3**, 703 (2004).
- <sup>69</sup>D. A. Baker, M. A. Paesler, G. Lucovsky, S. C. Agarwal, and P. C. Taylor, *Phys. Rev. Lett.* **96**, 255501 (2006).
- <sup>70</sup>L. Pauling, *The Nature of the Chemical Bond* (Cornell University Press, New York, 1939).
- <sup>71</sup>M. Wuttig, D. Lüsebrink, D. Wamwangi, W. Welnic, M. Gilleßen, and R. Dronskowski, *Nature Mater.* **6**, 122–128 (2006).
- <sup>72</sup>J.-P. Gaspard and R. Ceolin, *Solid State Commun.* **84**, 839 (1992).
- <sup>73</sup>M. Seo, J. Kim, H. Oh, M. Kim, I. Baek, K. Choi, J. Byun, and M. Lee, *Adv. Opt. Mater.* **7**, 1900196 (2019).
- <sup>74</sup>J. J. Bender, B. L. V. Bak, S. M. Jensen, and E. Lindgaard, *Compos. B Eng.* **217**, 108905 (2021).
- <sup>75</sup>T. Kim, J. Lee, Y. Kim, Y. Joo, and B. Kim, *Materials* **12**, 2490 (2019).
- <sup>76</sup>L. Mao, Q. Meng, A. Ahmad, and Z. Wei, *Adv. Energy Mater.* **7**, 1700535 (2017).
- <sup>77</sup>H. Zhu, Q. Li, C. Tao, Y. Hong, Z. Xu, W. Shen, S. Kaur, P. Ghosh, and M. Qiu, *Nat. Commun.* **12**, 1805 (2021).
- <sup>78</sup>K.-K. Du, Q. Li, Y.-B. Lyu, J.-C. Ding, Y. Lu, Z.-Y. Cheng, and M. Qiu, *Light Sci. Appl.* **6**, e16194 (2017).
- <sup>79</sup>K. Tang, K. Dong, J. Li, M. P. Gordon, F. G. Reichertz, H. Kim, Y. Rho, Q. Wang, C.-Y. Lin, C. P. Grigoropoulos, A. Javey, J. J. Urban, J. Yao, R. Levinson, and J. Wu, *Science* **374**, 1504–1509 (2021).
- <sup>80</sup>J. Wang, B. Xiong, R. Peng, C. Li, B. Hou, C. Chen, Y. Liu, and M. Wang, *Small* **17**, 2101282 (2021).
- <sup>81</sup>R. Song, Y. Zhang, Y. Zhang, J. Ma, L. Wu, and L. Song, *Appl. Phys. Express* **16**, 042001 (2023).
- <sup>82</sup>X. Jiang, X. Wang, J. Nong, G. Zhu, X. He, T. Du, H. Ma, Z. Zhang, H. Chen, Y. Yu, D. Liu, P. Yan, J. Wu, Z. Zhang, and J. Yang, *ACS Photonics* **11**, 218–229 (2024).
- <sup>83</sup>F. Chen, Y. Liu, X. Liu, and Y. Zheng, *Appl. Phys. Lett.* **122**, 191702 (2023).